

# Self-trapped electrons and self-trapped holes in PbBr<sub>2</sub> crystals

Masanobu Iwanaga

*Graduate School of Human and Environmental Studies, Kyoto University, Kyoto 606-8501, Japan*

Junpei Azuma, Masanobu Shirai, and Koichiro Tanaka

*Department of Physics, Graduate School of Science, Kyoto University, Kyoto 606-8502, Japan*

Tetsusuke Hayashi

*Faculty of Integrated Human Studies, Kyoto University, Kyoto 606-8501, Japan*

(Dated: December 2, 2024)

We have directly observed self-trapped electrons and self-trapped holes in PbBr<sub>2</sub> crystals with electron-spin-resonance (ESR) technique. The self-trapped states are induced below 8 K by two-photon interband excitation with pulsed 120-fs-width laser light at 3.10 eV. Spin-Hamiltonian analyses of the ESR signals have revealed that the self-trapping electron centers are the dimer molecules of Pb<sub>2</sub><sup>3+</sup> along the crystallographic *a* axis and the self-trapping hole centers are those of Br<sub>2</sub><sup>-</sup> with two possible configurations in the unit cell of the crystal. Thermal stability of the self-trapped electrons and the self-trapped holes suggests that both of them are related to the blue-green luminescence band at 2.55 eV coming from recombination of spatially separated electron-hole pairs.

PACS numbers: 71.20.Ps, 71.23.An, 71.38.Ht, 71.38.Mx

## I. INTRODUCTION

Strong electron-phonon interaction has been investigated theoretically<sup>1</sup> and experimentally in ionic crystals, especially in alkali halide crystals.<sup>2</sup> In the crystals, only the holes strongly interact with acoustic phonons and get self-trapped, forming the intrinsic hole centers of (halogen)<sub>2</sub><sup>-</sup>, while the electrons do not relax into self-trapped states. On the other hand, both electron-phonon and hole-phonon strongly interacting systems have not been found. Self-trapping of both electrons and holes was only studied theoretically and the uncommon relaxation was predicted;<sup>3</sup> the acoustic phonons strongly coupled with electrons and holes realize the repulsive correlation between the electron-hole (*e-h*) pairs, and the *e-h* pairs relax into individual self-trapped states. To find and examine the relaxation of the repulsive bipolarons with opposite charge, heavy metal halides can be considered as the candidates. Indeed, the excited states tend to have the instability resulting in the dimerization of halogen anions via a hole and the heavy metals enhance this tendency.<sup>4</sup> Because heavy metal cations often become electron traps,<sup>5</sup> the instability is suggestive of the *e-h* separation associated with local lattice deformation and of the individual self-trapping.

Lead halide, PbBr<sub>2</sub> and PbCl<sub>2</sub>, crystals decompose photochemically under ultraviolet (UV) light irradiation at room temperature.<sup>6</sup> At low temperatures, intense photoluminescence (PL) with large Stokes shift is induced instead of the photochemical decomposition.<sup>7,8</sup> Because ionic conductivity is suppressed at low temperatures, it is thought that local lattice deformation just after photoexcitation does not induce further successive desorption of halogen ions and aggregation of lead ions. The local lattice deformation is most likely related to the PL at low temperatures. These phenomena imply the strong

electron-phonon interaction in PbBr<sub>2</sub> and PbCl<sub>2</sub>.

By studying the PL properties at low temperatures below 30 K in PbBr<sub>2</sub>, it has been strongly suggested that bound and free *e-h* pairs intrinsically relax into spatially separated pairs of a self-trapped electron (STEL) and a self-trapped hole (STH).<sup>9,10</sup> The relaxation probably results from the strong interaction of both electrons and holes with acoustic phonons.<sup>3</sup> To obtain further insight into the relaxation of *e-h* pairs, it is significant to investigate structurally the lattice-relaxed localized states with electron-spin-resonance (ESR) technique in PbBr<sub>2</sub> photoirradiated at  $T \leq 30$  K.

Structures of localized electronic states have been investigated so far in other ionic crystals. In x-ray irradiated crystals of alkali halides, ESR experiments have revealed that the holes localize on two nearest-neighbor halogen ions and form the dimer molecules of (halogen)<sub>2</sub><sup>-</sup> (Refs. 2 and 11). The top of the valence band is composed of *np* states in *X*<sup>-</sup> ions (*X* = F, Cl, and Br for *n* = 2, 3, and 4, respectively), and the formation of the dimer-molecular STH is mainly attributed to the covalent bond of the *np* states.<sup>12</sup> On the other hand, holes in cubic PbF<sub>2</sub> irradiated with  $\gamma$  ray or neutrons localize on Pb<sup>2+</sup> ions and form Pb<sup>3+</sup> centers at  $T \leq 77$  K.<sup>13</sup> Some calculations<sup>14,15</sup> for cubic PbF<sub>2</sub> have indicated that the top of valence band is mainly composed of 6*s* states in Pb<sup>2+</sup>. The STH structure is closely related to the valence-band structure. Moreover, Pb<sup>2+</sup> ions can be effective hole traps and form Pb<sup>3+</sup> centers in Pb-doped alkali halide.<sup>16</sup>

STEL's were first observed in PbCl<sub>2</sub> irradiated with x ray<sup>17</sup> or  $\gamma$  ray<sup>18</sup> at about 80 K; the STEL's form the dimer molecules of Pb<sub>2</sub><sup>3+</sup> which are complementary to X<sub>2</sub><sup>-</sup> (V<sub>k</sub> center) in alkali halides, and the configuration is due to the conduction band composed of 6*p* states in Pb<sup>2+</sup> ions<sup>15</sup> and to the covalent bond of the 6*p* states. It

was proposed that STH's in  $\text{PbCl}_2$  form  $V_k$ -type  $\text{Cl}_2^-$  centers,<sup>19</sup> but the existence has been disputable. Although no definite experimental evidence simultaneously observing both STEL's and STH's has been reported so far,  $\text{PbCl}_2$  and  $\text{PbBr}_2$  are the candidates for yielding them.<sup>20</sup> The coexistence of STEL's and STH's gives the evidence that both electrons and holes strongly interact with phonons, and provides the experimental foundation for the further study on the uncommon relaxation of  $e$ - $h$  pairs.<sup>9,10,20</sup>

In order to clarify the relaxed states of  $e$ - $h$  pairs in  $\text{PbBr}_2$ , we have measured ESR signals induced with pulsed 120-fs-width and 3.10-eV laser light below 8 K. Spin-Hamiltonian analyses of the ESR signals have revealed that both electrons and holes get self-trapped and respectively form dimer molecules of  $\text{Pb}_2^{3+}$  and of  $\text{Br}_2^-$  as the self-trapping centers. We present the properties of ESR signals of  $\text{PbBr}_2$  and the thermal stability in Sec. III, analyze the structures of the electron-trapping and the hole-trapping centers with spin Hamiltonians in Sec. IV, and discuss the correlation of STEL's and STH's with luminescence in Sec. V.

## II. EXPERIMENTAL PROCEDURES

Single crystal of  $\text{PbBr}_2$  was grown with the Bridgman technique from 99.999% powder purified under vacuum distillation. The crystal of orthorhombic  $D_{2h}^{16}$  (Refs. 21 and 22) was cut in the size of  $3 \times 3 \times 3 \text{ mm}^3$  along the right-angled crystallographic  $a$ ,  $b$ , and  $c$  axes.

The crystal was sealed in a transparent quartz capillary with a transparent quartz rod and was fixed in a microwave cavity with a guide for light injection. The microwave cavity was a rectangular  $\text{TE}_{103}$  cavity resonator with the quality factor  $Q = 3000$ . The sample was photoirradiated below 8 K with the second harmonics (pulsed 120-fs-width, 1-kHz, and 3.10-eV light) generated from a regeneratively amplified Ti:sapphire laser; the average power of the incident light was about 100  $\text{mW}/\text{cm}^2$  on the sample surface and the photoirradiation time was typically one hour. The incident photons induce the two-photon interband transition, create  $e$ - $h$  pairs almost uniformly in the crystal, and produce measurable ESR signals within one minute. To avoid optical bleaching of the ESR signals, the sample after photoirradiation was kept dark during the measurement.

The photoirradiated sample was measured below 8 K with ordinary ESR technique in X-band range; the resonant microwave frequency was  $9.378(\pm 0.008) \text{ GHz}$ . Rotation-angle dependence of the ESR signals was measured by rotating the crystal around the  $a$ ,  $b$ , and  $c$  axes. Thermoluminescence (TL) under pulse annealing was measured through the transparent quartz rod attached to the sample. The total TL during the pulse annealing were directly detected by a photomultiplier, and the TL spectra at various pulse-annealing temperatures were measured with a charge-coupled device cam-

era equipped with a grating monochromator. Raising- and lowering-rates of temperature under pulse annealing were about 5 K/s, and the sample was typically annealed for one second at each annealing temperature. The ESR spectra after pulse annealing were measured below 8 K.

## III. EXPERIMENTAL RESULTS

### A. Properties of ESR spectra

Figure 1 shows a typical ESR spectrum measured at 5 K after photoirradiation at 5 K. The solid lines in Fig. 1 indicate the prominent ESR positions and the dashed lines do the ESR positions calculated from the spin Hamiltonians in Sec. IV. The signals are classified into three groups by the rotation-angle dependence and the thermal profiles: (i) The ESR signals named as STEL survive up to 130 K under pulse annealing. (ii) The signals named as STH disappear under pulse annealing at  $T \geq 30 \text{ K}$ . (iii) Though the several signals in 280-340 mT cannot be well resolved because of the overlap with the STH signals, they survive above 100 K and almost disappear around 130 K under pulse annealing. The signals named as STEL and STH respectively correspond to self-trapped electrons and self-trapped holes, as analyzed with spin Hamiltonians in Secs. IV A and IV B. ESR signals around 330 mT under UV light irradiation at 77 K were reported by several authors.<sup>23,24,25</sup> However, the ESR signals named as STEL and STH have not been reported to our knowledge. Because of the overlap of the ESR signals, the spectrally well-resolved STEL and STH signals are mainly restricted to the region higher than 340 mT; in the region the intensity ratio of the STEL signals is 4 : 1 and that of the STH signals is 3 : 2 : 1. The STEL signals show linear response to the microwave power up to 10 mW even at 5 K. On the other hand, the STH signals saturate for the microwave power higher than 0.01 mW at 6 K. The reduced line width of the STEL signals,  $\Delta B = (g/g_0)\Delta B_0$  is estimated to be  $14(\pm 1) \text{ mT}$  where  $g$  is the  $g$  value of the STEL,  $g_0$  the free-electron  $g$  factor, and  $\Delta B_0$  the line width estimated from the experimental data; the  $\Delta B$  is about three-times broader than  $\Delta B = 5.5 \text{ mT}$  in  $\text{PbCl}_2$  (Ref. 17).

Figure 2 presents the rotation-angle dependence of the STEL signals (closed circle) at 8 K; magnetic field vector  $\mathbf{B}$  is in the  $ab$  plane and the rotation axis is the  $c$  axis. Index  $(I, M_I)$  denotes the pair of the total nuclear spin of the STEL center and the magnetic quantum number. The intensities of the ESR signals with indexes  $(1, 0)$  and  $(1, -1)$  are more than ten-times as weak as the  $(0, 0)$ . The intensity ratio between  $(0, 0)$ ,  $(1/2, 1/2)$ , and  $(1/2, -1/2)$  is about 4 : 0.9 : 1. Solid and dashed lines fit the experimental data and are derived from the spin Hamiltonian (1) in Sec. IV A. A similar rotation-angle dependence of the STEL in  $\text{PbCl}_2$  shows the twofold splits when the  $\mathbf{B}$  is in the  $bc$  and the  $ac$  planes;<sup>17,18</sup> the splits come from the two configurations reflecting the crystallographic symme-

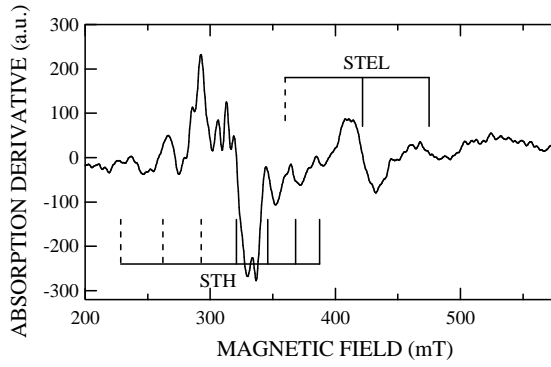


FIG. 1: Typical ESR spectrum measured at 5 K aft

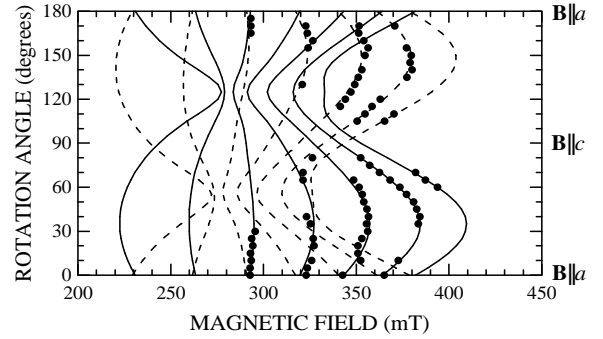


FIG. 3: Photoinduced STH signals (closed circle) vs rotation angle measured at 8 K. Microwave frequency is  $9.383(+0.002)$

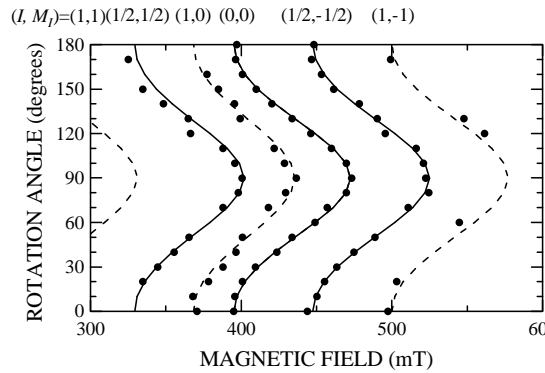


FIG. 2: Photoinduced STEL signals (closed circle) vs r angle measured at 8 K. Microwave frequency is  $9.371(-)$  GHz. Magnetic field vector  $\mathbf{B}$  is in the  $ab$  plane and tl tion axis is the  $c$  axis.  $(I, M_I)$ : the total nuclear spir STEL centers and the magnetic quantum number. Sc dashed lines: fitting lines derived from the spin Hamil described in Sec. IV A.

try. However, the explicit split has not been obser  $\text{PbBr}_2$  when the  $\mathbf{B}$  is in the  $bc$  and the  $ac$  planes. ably, the broad line width in  $\text{PbBr}_2$  hides the split

Figure 3 displays the rotation-angle dependence STH signals (closed circle); the magnetic field vec is in the  $ac$  plane and the rotation axis is the  $b$  axis signals are picked up from the ESR spectra as ; in Fig. 1. There exist the two series each of which more than three resonances. The two series are 1 symmetric for the  $bc$  plane with each other, reflecti crystallographic mirror symmetry. Solid and dashe are derived from the spin Hamiltonian describing th center composed of two-equivalent  $\text{Br}^-$  ions, and t STH signals.

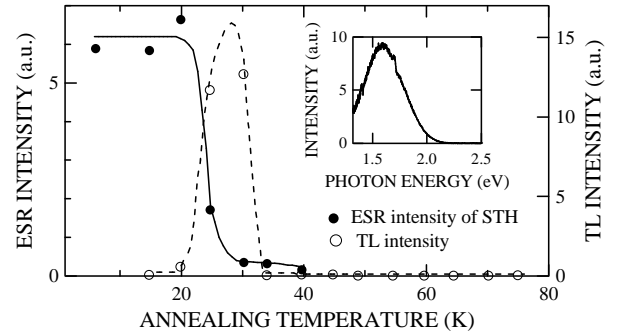


FIG. 4: ESR intensity of the STH signals (closed circle) and total TL intensity during pulse annealing (open circle). The abscissa stands for pulse-annealing temperature. The ESR signals after pulse annealing were measured at 6 K. Solid and dashed lines are drawn for guides to the eye. The inset displays the TL spectrum under pulse annealing at 22 K.

## B. Thermal stability of ESR signals and thermoluminescence

Figure 4 shows the thermal stability of the STH signals (closed circle) and the total TL intensity during the pulse annealing (open circle). The ESR signals after pulse annealing were measured at 6 K. The intensity of the STH signals sharply decreases above 20 K and the signals were hardly observed after pulse annealing at 40 K. The ESR signals in 280-340 mT also decrease up to 40 K by the similar amount to the STH signals, and keep almost constant under pulse annealing at 40-100 K. TL appears corresponding to the quenching of the STH signals over 20-30 K. The TL spectrum under pulse annealing at 22 K is displayed in the inset of Fig. 4. The TL spectrum at 1.6 eV is spectrally in agreement to the red PL band; it is induced under excitation into the fundamental absorption region and increases in 20-30 K instead of the decrease of blue-green PL band at 2.55 eV.<sup>9,10</sup>

Figure 5 shows the stability of the STEL signals (closed

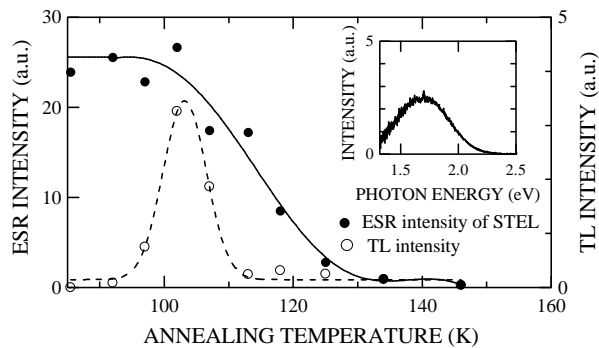


FIG. 5: ESR intensity of the STEL signals (closed circle) and total TL intensity during pulse annealing (open circle). The abscissa stands for pulse-annealing temperature. The ESR signals after pulse annealing were measured at 5 K. Solid and dashed lines are drawn for guides to the eye. The inset displays the TL spectrum measured around the peak of the TL curve (dashed line).

circle) and the total TL intensity during the pulse annealing (open circle). The ESR signals after pulse annealing were measured at 5 K. The intensity of the STEL signals decreases above 100 K and the signals are quenched at 145 K. The ESR signals in 280-340 mT also vanish together with the STEL signals. TL was observed over 90-140 K, strongly in 100-105 K. The TL spectrum measured around the peak of the TL curve is displayed in the inset of Fig. 5; the TL spectrum peaks at 1.7 eV and is located in the high-energy side in comparison with the spectrum in Fig. 4. The TL spectrum in Fig. 5 is spectrally in agreement with the PL spectrum in this temperature range. The PL has the extrinsic nature;<sup>26</sup> it is induced under excitation even in the energy range ( $\hbar\omega \geq 3.5$  eV) lower than the fundamental absorption edge of 3.8 eV.<sup>10</sup>

#### IV. SPIN-HAMILTONIAN ANALYSIS

##### A. Structure of self-trapped electrons

The ESR signals prominently appeared in 410-530 mT have the  $g$  value of  $g < 2$  and therefore are ascribed to electron centers.<sup>27</sup> They have the similar rotation-angle dependence with each other as shown in Fig. 2, and thermally disappear together. The intensity ratio seems to reflect the isotope effect. Indeed,  $\text{Pb}^{2+}$  ions are consisted of nuclear spin  $I = 0$  (contained 79% naturally) and  $I = 1/2$  (contained 21% naturally). The pair of two-equivalent Pb-ions has the total nuclear spin of 0 (singlet), 1/2 (doublet), and 1 (triplet); the constituent ratio is 19.2 : 10 : 1. When the degeneracy of the multiplets is lifted, the ratio of the singlet to the two doublets is 19.2 : 5 : 5  $\approx$  4 : 1 : 1. This ratio is in agreement with the ratio 4 : 0.9 : 1 estimated from Figs. 1 and 2, and moreover it is probable that the far weak signals fitted

with dashed lines in Fig. 2 come from the nondegenerated triplets.

Therefore, one can assume that an electron equivalently localizes on two nearest-neighbor  $\text{Pb}^{2+}$  ions and they form a  $\text{Pb}_2^{3+}$  center. The spin Hamiltonian  $\mathcal{H}$  with Zeeman and hyperfine terms is given by

$$\mathcal{H} = \mu_B \mathbf{S} \cdot \underline{g} \cdot \mathbf{B} + g_0 \mu_B \mathbf{I}_1 \cdot \underline{A}_1 \cdot \mathbf{S} + g_0 \mu_B \mathbf{I}_2 \cdot \underline{A}_2 \cdot \mathbf{S}, \quad (1)$$

where  $\mu_B$  denotes the Bohr magneton,  $\mathbf{S}$  the electron spin,  $\underline{g}$  the Zeeman tensor,  $\mathbf{B}$  magnetic field vector,  $g_0$  the free-electron  $g$  factor,  $\mathbf{I}_i$  the nuclear spin, and  $\underline{A}_i$  the hyperfine tensor ( $i = 1, 2$ ). The Pb-ion dimer does not contain the nuclear quadrupole term because  $I_i = 0$  or  $1/2$ . In addition, the nuclear Zeeman term is omitted because the contribution is small enough, compared to that of the electron Zeeman and the hyperfine terms. For the spin Hamiltonian without the quadrupole and the nuclear Zeeman terms, the total nuclear spin  $I$  ( $\mathbf{I} = \mathbf{I}_1 + \mathbf{I}_2$ ) and  $M_I$  ( $M_I = I, I - 1, \dots, -I$ ) become good quantum numbers.<sup>28</sup>

Each rotation-angle series of the ESR signals in Fig. 2 takes maximum and minimum values when the  $\mathbf{B}$  is parallel to the crystallographic axes, that is, when  $\mathbf{B} \parallel a$  and  $\mathbf{B} \parallel b$ . Under the condition that the  $\mathbf{B}$  is in the  $bc$  and the  $ac$  planes, the ESR signals also show a similar rotation-angle dependence. The dependence justifies the assumption that the principal  $g$  axes are coincident with the crystallographic axes. Moreover, because the rotation-angle dependence of  $(1/2, \pm 1/2)$  is similar to that of  $(0, 0)$ , one can assume the agreement of the principal axes of  $A$  tensor with those of  $g$  tensor. Thus, we set the principal  $g$  and  $A$  axes such as  $x = c$ ,  $y = b$ , and  $z = a$ .

The direction of radius in polar coordinate  $(r, \theta, \phi)$  is chosen to be that of the magnetic field vector  $\mathbf{B}$ . Under axial symmetry ( $A_x = A_y$ ) and the second-order perturbation taking Zeeman term as the unperturbed term and hyperfine terms as the perturbed term, the Hamiltonian (1) is transformed to eq. (2), describing the allowed ESR transitions such as  $\Delta M_S = 1$ ,  $\Delta I = 0$ , and  $\Delta M_I = 0$ . The axial symmetry implies that the dimer-molecular axis is chosen to be the  $z$  axis. Equation (2) is finally represented in mT with  $(\theta, \phi)$ ;<sup>28</sup>

$$\Delta \mathcal{H} = (g_0/g) \{ B_0 - AM_I - (D^2/2B_0)M_I^2 - [(B^2 + C^2)/4B_0][I(I+1) - M_I^2] \}, \quad (2)$$

where

$$\Delta \mathcal{H} = \langle +|\mathcal{H}|+ \rangle - \langle -|\mathcal{H}|- \rangle,$$

$$|\pm \rangle = |M_S = \pm 1/2 \rangle,$$

$$g_0 = 2.0023,$$

$$g = \sqrt{g_z^2 \cos^2 \theta + g_\perp^2 \sin^2 \theta},$$

$$g_\perp = \sqrt{g_x^2 \cos^2 \phi + g_y^2 \sin^2 \phi},$$

$$B_0 = h\nu/g_0\mu_B \quad (\nu: \text{microwave frequency}),$$

$$\begin{aligned}
I &= I_1 + I_2, I_1 + I_2 - 1, \\
M_I &= I, I - 1, \dots, -I, \\
A^2 &= (1/g^2)[A_z^2 g_z^2 \cos^2 \\
A_{\perp}^2 &= (1/g_{\perp}^2)[A_x^2 g_x^2 \cos^2 \\
B &= A_z A_{\perp} / A, \\
C &= A_{\perp}, \\
D &= (g_z g_{\perp} / g^2)(A_{\perp}^2 - A^2)
\end{aligned}$$

Equation (2) well describes dependent series of the ESR signals as in Fig. 2. For  $I = 0$ , the Hanman term, and the principal  $g$  fitting the series of the largest signal  $(I, M_I) = (0, 0)$  in Fig. 2 relate. Principal  $A$  values are of  $I = 1/2$ , using the principal with indexes  $(1/2, 1/2)$  and  $(1, 0)$  series by varying the principal lines in Fig. 2 are drawn with those with  $(1, 0)$  and  $(1, -1)$  dependence. Analysis confirms that the ESR spectrum named as STEL in Fig. 1 and the ESR signals in Fig. 2 originate from the electron-trapping center of  $\text{Pb}_2^{3+}$ . As for the electron centers, it is improbable that they are affected by vacancies or impurities because the rotation-angle dependence excludes the symmetry breaking around the electron centers by the permanent lattice defects. The coexistence of STEL's and "perturbed" STEL's by the defects is also excluded because of the single rotation-angle pattern and the thermal decay. In addition, the electron centers are readily, within one minute, produced under photoirradiation. The production profile is also suggestive of the simple electron centers like  $\text{Pb}_2^{3+}$ . Therefore, the electron centers named as STEL in Fig. 1 are finally declared to be self-trapping electron centers of  $\text{Pb}_2^{3+}$ .

The structures of the STEL centers are schematically shown in Fig. 6; among the two nearest-neighbor Pb-ion pairs, the pairs along the  $a$  axis are the configurations consistent with the analysis unfolded in this section. In Fig. 6, each stick which bonds the two  $\text{Pb}^{2+}$  ions stands for the covalent bond via the localized electron. As described in Sec. III A, the broad line width of the STEL signals probably hides the twofold splits in the  $ab$  and the  $ac$  planes observed in  $\text{PbCl}_2$  (Refs. 17 and 18), and consequently the  $x$  and  $y$  axes determined here may deviate slightly from the principal  $x$  and  $y$  axes corresponding to each of the twofold splits.

The principal values of Zeeman  $g$  and hyperfine  $A$  tensors are listed in Table I; the principal  $g$  values take 1.4-1.7 and are comparable to the values of  $\text{Pb}_2^{3+}$  in  $\text{PbCl}_2$  and  $\text{NaCl:Pb}$ .<sup>17,18,29</sup> This analysis only provides the absolute values of  $A_x$ ,  $A_y$  and  $A_z$ , and the principal  $A$  values are in the same order of several tens mT as in  $\text{PbCl}_2$  and  $\text{NaCl:Pb}$ . In accordance with  $\text{Pb}_2^{3+}$  in  $\text{PbCl}_2$  and  $\text{NaCl:Pb}$ , the same signs of principal  $A$  values are chosen for  $\text{Pb}_2^{3+}$  in  $\text{PbBr}_2$ . The parameters  $\rho_s$  and  $A_{\sigma}$  of  $\text{PbBr}_2$  are calculated with the  $g$  and the  $A$  values in the

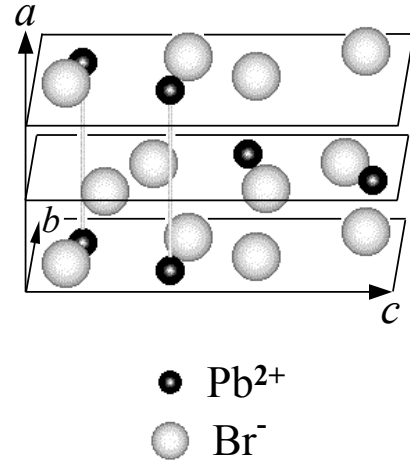


FIG. 6: Schematic configurations of the electron-self-trapping  $\text{Pb}_2^{3+}$  center in  $\text{PbBr}_2$  crystal. Four  $\text{Pb}^{2+}$  ions (small black ball) and eight  $\text{Br}^-$  ions (large white ball) in the two nearest-neighbor  $bc$  planes constitute the unit cell of the crystal. The lengths of the unit cell along the  $a$ ,  $b$ , and  $c$  axes are 4.767, 8.068, and 9.466 Å, respectively (Ref. 21). There exist the two configurations of the STEL centers in the crystal, and each STEL center of  $\text{Pb}_2^{3+}$  is schematically represented with the two nearest-neighbor  $\text{Pb}^{2+}$  ions along the  $a$  axis and the stick which depicts the covalent bond of the two  $\text{Pb}^{2+}$  ions via the electron. The spin-Hamiltonian parameters of the  $\text{Pb}_2^{3+}$  center are listed in Table I.

perturbative analysis for the electronic levels of dimer-molecular centers.<sup>12,29</sup> The physical meanings of the  $\rho_s$  and the  $A_{\sigma}$  are discussed in Sec. V B.

## B. Structures of self-trapped holes

The three prominent ESR signals in 350-390 mT named as STH in Fig. 1 belong to the series with the similar rotation-angle dependence and the same thermal stability under pulse annealing. The intensity of the ESR signals in 280-340 mT decrease up to 40 K by the similar amount to the three signals in 350-390 mT. Therefore, there probably exist further signals in 280-340 mT of the same origin with the three signals in 350-390 mT, though the overlap with other signals prevents from observing them separately. The ESR signals in 280-390 mT have the  $g$  values of  $g \approx 2$  and probably originate from hole centers.<sup>27</sup>

In  $\text{PbBr}_2$ , we assume two-equivalent-nuclei  $\text{Br}_2^-$  as the hole center with more than three resonances in 280-390 mT. This assumption is consistent with the ratio of 3 : 2 : 1 estimated in Fig. 1; full signals of  $\text{Br}_2^-$  would be composed of seven resonances with the ratio of 1 : 2 : 3 : 4 : 3 : 2 : 1 in the first-order hyperfine effect associated with the Br-nuclear spin of 3/2.

The spin Hamiltonian  $\mathcal{H}$  is also expressed by eq. (1). For  $\text{Br}_2^-$ , quadrupole term can be added as a second-order effect<sup>28</sup> because the nuclear spin of  $\text{Br}^-$  is 3/2.

TABLE I: Spin-Hamiltonian parameters of  $\text{Pb}_2^{3+}$  electron centers. Principal  $A_i$  values ( $i = x, y, z$ ),  $\rho_s$ , and  $A_\sigma$  are represented in mT. The meanings of  $\rho_s$  and  $A_\sigma$  are discussed in Sec. V B. The parameters of  $\text{Pb}_2^{3+}$  centers in  $\text{PbCl}_2$  and  $\text{NaCl:Pb}$  are also cited for comparison.

Electron center	$g_x$	$g_y$	$g_z$	$A_x$	$A_y$	$A_z$	$\rho_s$	$A_\sigma$
$\text{Pb}_2^{3+}$ in $\text{PbBr}_2^a$	1.563 $\pm 0.002$	1.416 $\pm 0.002$	1.690 $\pm 0.002$	-87 $\pm 4$	-87 $\pm 3$	100 $\pm 5$	39	-14
$\text{Pb}_2^{3+}$ in $\text{PbCl}_2^b$	1.549 $\pm 0.001$	1.379 $\pm 0.001$	1.718 $\pm 0.003$	-85 $\pm 1$	-85 $\pm 1$	109 $\pm 1$	39	-5
$\text{Pb}_2^{3+}$ in $\text{PbCl}_2^d$	1.494 $\pm 0.005$	1.322 $\pm 0.005$	1.662 $\pm 0.005$	NR <sup>c</sup>	NR	NR	NR	NR
$\text{Pb}_2^{3+}$ in $\text{NaCl:Pb}^e$	1.469 $\pm 0.002$	1.300	1.621	-115	-123	115	46	-29

<sup>a</sup>This work; Sec. IV A.

<sup>b</sup>Reference 17.

<sup>c</sup>Not reported.

<sup>d</sup>Reference 18.

<sup>e</sup>References 17 and 29.

However, explicit second-order served in our measurements. T (1) containing only first-order data and moreover hypothesized pal  $g$  and  $A$  axes.

As shown in Fig. 3, the solid series are mirror symmetric for rotation-angle dependences in  $g$  and  $A$  axes deeply tilt from  $z$ . This deviation and the overlap in mT make it difficult to determine principal  $x$ ,  $y$ , and  $z$  axes. However, we determine approximately the  $z$  axis from the well-resolved signals in 350 and 390 mT and second Euler angles are respectively  $129^\circ$  and  $126^\circ$  for the dashed series fitted with the solid line. The  $z$  axis cannot be determined experimentally to be  $0^\circ$ , and consequent  $x$  and  $y$  axes determined here are not with the principal  $x$  and  $y$  axes.

Equation (1) is transformed under the same approximation. The allowed ESR transitions are described with eq. (2) except for  $I = 3$ . Equation (2) describes the rotation-angle dependence of the three prominent signals in 350-390 mT and other prominent signals in  $B \leq 340$  mT. Table II presents the principal  $g$  and  $A$  values obtained by the fitting and shows that the values of  $\text{Br}_2^-$  centers in  $\text{PbBr}_2$  are comparable to those in alkali bromides. Though this spin-Hamiltonian analysis cannot provide the signs of hyperfine parameters  $A_x$ ,  $A_y$ , and  $A_z$ , the molecular analysis<sup>12</sup> of electronic levels in  $\text{Br}_2^-$  centers requires the signs to be positive, and the same signs are chosen in  $\text{PbBr}_2$  in accordance with the analysis. The parameters  $\rho_s$  and  $A_\sigma$  in Table II are discussed in comparison with those of other host crystals in Sec. V B.

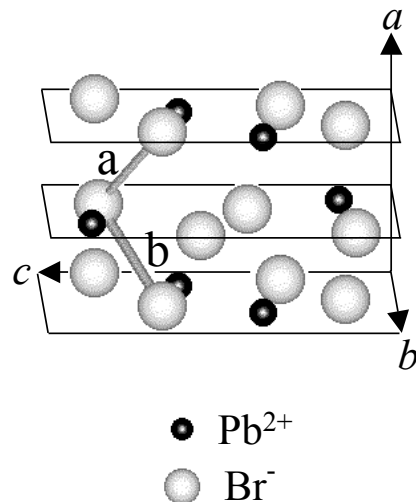


FIG. 7: Schematic configurations of the hole-self-trapping  $\text{Br}_2^-$  centers in  $\text{PbBr}_2$  crystal.  $\text{Br}_2^-$  is composed of two  $\text{Br}^-$  ions (large white ball) and one hole. Each stick schematically represents the covalent bonds of two  $\text{Br}^-$  ions via the hole. The two dimer-molecular  $\text{Br}_2^-$  named as a and b respectively correspond to the solid-line and the dashed-line series in Fig. 3. Two  $\text{Pb}^{2+}$  ions (small black ball) and four  $\text{Br}^-$  ions are sited in each  $bc$  plane. The spin-Hamiltonian parameters of the  $\text{Br}_2^-$  centers (the pairs a and b) are listed in Table II.

The  $\text{Br}$ -ion pairs whose axis is in agreement with the principal  $z$  axis of the solid-line series in Fig. 3 are limited to the pair a in Fig. 7; for the pair a, the first and second Euler angles of the molecular axis are respectively  $50.7^\circ$  and  $126.1^\circ$  when the lattice ions are located at the equilibrium positions. Similarly, the dashed-line series in Fig. 3 correspond to the pair b in Fig. 7; the first and second Euler angles are  $129.3^\circ$  and  $126.1^\circ$ , respectively. The pairs a and b are indeed mirror symmetric for the  $bc$

plane.

The good agreement of the dimer-molecular axes with the direction of the Br-ion pairs in the crystal confirms that the STH signals originate from the  $\text{Br}_2^-$  centers which are not affected by any permanent lattice defect. Therefore, the hole centers named as STH in Sec. III A are ascribed to the self-trapping hole centers of  $\text{Br}_2^-$ .

## V. DISCUSSION

### A. Correlation of self-trapped states with luminescence

Thermal stability of the ESR signals indicates that the STEL's and the STH's coexist only in the temperature range of  $T \leq 30$  K. Therefore, intrinsic luminescence related to both STEL's and STH's would appear in  $T \leq 30$  K.

Blue-green (BG) PL band at 2.55 eV is the dominant intrinsic PL at  $T \leq 20$  K in  $\text{PbBr}_2$ , and the phosphorescent decay is well described by the radiative recombination model.<sup>10</sup> The model assumes the process that the spatially separated  $e$ - $h$  pair gets close by tunneling motion, forms a self-trapped exciton (STE), and recombines with radiation. The phosphorescent decay suggests that the BG-PL band originates from the distant pairs of a STEL and a STH.

The BG-PL band thermally decreases in 20-30 K and disappears above 30 K.<sup>10</sup> The thermally stable range of the BG-PL band corresponds to that of both STEL's and STH's. These correspondence supports that the BG-PL band is closely related to both STEL's and STH's. In particular, the BG-PL band is not induced in the temperature range above 30 K, where the STH's disappear as shown in Fig. 4. Therefore, it is plausible that the STE's yielding the BG-PL have the configuration of  $(\text{Br}_2^- + \text{electron})$ , though it is unknown whether the STE is the nearest-neighbor pair of a STH and a STEL or has the configuration that a  $\text{Br}_2^-$  center bounds an electron in the excited orbital. On the other hand, the red PL band grows instead of the quenching of the BG-PL band in 20-30 K; as shown in Fig. 4, the temperature range corresponds to the growth of the red TL that has the same shape with the red PL band. Because of the instability of the STH centers in 20-30 K, the red PL and the red TL are ascribed to the STE's associated with the STEL centers of  $\text{Pb}_2^{3+}$  stable in 20-30 K. To clarify the configurations of the self-trapped excitons directly, the examination with optically detected magnetic resonance technique is preferable, because this ESR study can only suggest the configurations of the STE's yielding the BG-PL and the red PL bands.

As for the thermal stability of self-trapping centers, it is to be noted that the temperature where the STH's and the STEL's disappear under pulse annealing does not necessary indicate that of the thermal quenching of the self-trapping centers itself. Indeed, the thermal de-

cay of  $\text{Br}_2^-$  in alkali halides is affected by the thermal activation of trapped electrons and positive vacancies.<sup>12</sup> In  $\text{PbBr}_2$ , vacancies of  $\text{Br}^-$  and  $\text{Pb}^{2+}$  inevitably exist because of the high ionic conductivity,<sup>30,31</sup> and the density of  $\text{Br}^-$  vacancy is estimated at more than  $10^{17} \text{ cm}^{-3}$ . Consequently, it is likely that the thermal activation of vacancies affects the STH's: (i) it makes the self-trapped states unstable, induces the thermal transfer of the holes, and leads the holes to radiative and/or nonradiative decay, or (ii) it deforms the self-trapping centers to other trapping centers associated with vacancies. The thermal stability of the STEL's may be also affected by the thermal activation of other hole centers as discussed in Sec. V C.

### B. Electronic structures of self-trapped centers

In this section we tentatively apply the perturbative analysis in Refs. 12 and 29 to the dimer centers, and discuss the electronic structures of STEL's and STH's in  $\text{PbBr}_2$  from the comparison with other crystals.

According to the analysis,<sup>12,29</sup> the mixing by spin-orbit interaction between the ground  $\sigma_g$  and the excited orbitals  $\pi_g^x, \pi_g^y$  in the dimer molecule of  $\text{Pb}_2^{3+}$  and  $\text{Br}_2^-$  are calculated from the  $g$  shift and the principal  $A$  values under Hatree-Fock approximation and the second-order perturbation taking the spin-orbit interaction as the perturbed term. The parameters  $\rho_s$  in Tables I and II denote the dipole-dipole interaction between the magnetic moments of the electron (or hole) and nuclei, and represent the anisotropic contribution to the hyperfine term. The parameters  $A_\sigma$  represent the isotropic contribution to the  $A$  tensor and are given by  $A_\sigma = A_\sigma^s + A_\sigma^e$  where  $A_\sigma^s$  is the positive Fermi contact term and  $A_\sigma^e$  the negative exchange-polarization term of the inner electrons.

For  $\text{Pb}_2^{3+}$ ,  $A_\sigma^s$  is proportional to  $6s$ -state mixing into the ground orbital  $\sigma_g = \alpha_g(6s_1 + 6s_2) + \beta_g(6p_{1,z} - 6p_{2,z})$  where  $\alpha_g$  and  $\beta_g$  are constants, and  $6s$  and  $6p$  respectively denote the atomic wave functions of the  $6s$ - and the  $6p$ -states in  $\text{Pb}^{2+}$ .  $\rho_s$  is  $\rho_s \propto \beta_g^2 \langle r^{-3} \rangle$  where  $\langle r^{-3} \rangle$  is the spatial distribution of the electron, and the small  $\rho_s$  values result in the spread of the electron as long as the  $\beta_g$ 's of  $\text{Pb}_2^{3+}$  are comparable in different host crystals. As shown in Table I,  $\rho_s$  in  $\text{PbBr}_2$  has the same value with that in  $\text{PbCl}_2$  and 15% smaller than that in  $\text{NaCl:Pb}$ ; the  $\rho_s$  suggests that the distribution of STEL in  $\text{PbBr}_2$  spreads as outward as in  $\text{PbCl}_2$  and more outward than  $\text{NaCl:Pb}$ .  $A_\sigma$  in  $\text{PbBr}_2$  is negatively 2.8 times larger than that in  $\text{PbCl}_2$ . In other words, the positive part  $A_\sigma^s$ , which reflects  $6s$ -mixing into the ground orbital  $\sigma_g$ , contributes more than the negative  $A_\sigma^e$  in  $\text{PbCl}_2$ . This result qualitatively suggests that  $6s$ -mixing into the  $\sigma_g$  is larger in  $\text{PbCl}_2$  than in  $\text{PbBr}_2$ . The difference is probably ascribed to the components of the top of valence band. The valence-band structure of  $\text{PbCl}_2$  with more mixing of  $6s$ -states in  $\text{Pb}^{2+}$  ions may make it possible for the holes to form the STH centers of  $\text{Pb}^{3+}$  as observed in  $\text{PbF}_2$  (Ref.

TABLE II: Spin-Hamiltonian parameters of  $\text{Br}_2^-$  hole centers. Principal  $A_i$  ( $i = x, y, z$ ) values,  $\rho_s$ , and  $A_\sigma$  are represented in mT. The meanings of  $\rho_s$  and  $A_\sigma$  are discussed in Sec. VB. The parameters of  $\text{Br}_2^-$  centers in KBr, NaBr, and RbBr are cited for comparison.

Hole center	$g_x$	$g_y$	$g_z$	$A_x$	$A_y$	$A_z$	$\rho_s$	$A_\sigma$
$\text{Br}_2^-$ (pair a) <sup>a</sup>	2.16	2.17	1.90	10	10	46	16	17
in $\text{PbBr}_2$	$\pm 0.02$	$\pm 0.02$	$\pm 0.01$	$\pm 4$	$\pm 4$	$\pm 1$		
$\text{Br}_2^-$ (pair b) <sup>a</sup>	2.18	2.23	1.90	10	10	46	19	14
in $\text{PbBr}_2$	$\pm 0.05$	$\pm 0.05$	$\pm 0.03$	$\pm 1$	$\pm 1$	$\pm 7$		
$\text{Br}_2^-$ in $\text{NaBr}$ <sup>b</sup>	2.1514	2.1968	1.9791	6.50	7.38	43.1	18.23	12.66
$\text{Br}_2^-$ in $\text{KBr}$ <sup>b</sup>	2.1629	2.1623	1.9839	7.68	7.66	45.0	17.98	14.45
$\text{Br}_2^-$ in $\text{RbBr}$ <sup>b</sup>	2.1683	2.1524	1.9846	8.36	8.12	45.5	17.80	15.13

<sup>a</sup>This work; Sec. IV B.

<sup>b</sup>Reference 12; the accuracies of parameters  $g$  and  $A$  are within  $\pm 0.0005$  and  $\pm 0.07$ , respectively.

13). Indeed, the mixing ratios of the  $6s$ -states into the top of the valence bands become large in order of  $\text{PbBr}_2$ ,  $\text{PbCl}_2$ ,  $\text{PbF}_2$  (Ref. 15).

The complementary discussion can be applied to  $\text{Br}_2^-$ . Parameters  $\rho_s$  and  $A_\sigma$  in Table II are comparable to each other. This analysis implies that the distribution of STH and the orbital functions of the  $\sigma_g$  in  $\text{PbBr}_2$  are quite similar to those in alkali bromides.

### C. Other trapped centers associated with lattice defects

The ESR signals in 280-340 mT have the  $g$  values of  $g \geq 2$ , and the overlap of the signals prevents from discriminating each signal and analyzing with spin Hamiltonian. However, they vanish together with the STEL signals around 120 K under pulse annealing, and then the crystal emits TL as shown in Fig. 5. Therefore, the signals in 280-340 mT are most likely to originate from hole-trapping centers.

From the valence-band structure,  $\text{Pb}^{3+}$  center can be considered as another candidate for intrinsic hole-trapping center, but the satellites, which stem from the isotope  $^{207}\text{Pb}$  of  $I = 1/2$  (contained 21% naturally), have not been observed in 0-1 T just as seen in  $\text{PbF}_2$  crystals<sup>13</sup> and Pb-doped KCl crystals.<sup>16</sup> Interstitial lattice defects, namely, Frenkel defects have been also excluded in  $\text{PbBr}_2$ .<sup>30,31</sup> Consequently, the signals in 280-340 mT except for the unresolved STH signals probably originate from the extrinsic hole center associated with the permanent lattice defects such as vacancy or impurity or both. The extrinsic hole-trapping centers are efficient competitors of the STH centers because they survive above 100

K together with not a few STEL and disappear around 120 K with emitting TL.

## VI. CONCLUSIONS

Self-trapping electron and self-trapping hole centers are simultaneously photoinduced by two-photon inter-band excitation with 120-fs-width laser light at 3.10 eV and have been directly detected with ESR technique. The excitation enables to induce  $e$ - $h$  pairs with enough density for the present ESR measurements. Spin-Hamiltonian analyses have revealed that the structures of STEL's and STH's are the dimer-molecular  $\text{Pb}_2^{3+}$  and  $\text{Br}_2^-$ , respectively. The STEL centers of  $\text{Pb}_2^{3+}$  orient along the crystallographic  $a$  axis. The holes select self-trapping sites among many nearest-neighbor Br-ion pairs in the unit cell, and form the STH centers of  $\text{Br}_2^-$  with the two particular orientations. From the comparison of the principal  $g$  and  $A$  values, the  $\text{Pb}_2^{3+}$  and the  $\text{Br}_2^-$  centers are similar to those in other crystals studied so far.

From this ESR study, we conclude that both electrons and holes in  $\text{PbBr}_2$  crystals strongly interact with acoustic phonons and do relax into the individual self-trapped states.

Moreover, the STEL's and the STH's centers coexist at  $T \leq 30$  K, and the STH centers disappear in 20-30 K. The temperature range is in good agreement with the range where the phosphorescent blue-green PL band at 2.55 eV is induced. The agreement supports the conclusion of the previous PL study (Ref. 10) that both STEL and STH centers are related to the radiative recombination process yielding the blue-green PL band.

<sup>1</sup> Y. Toyozawa, in *Excitonic Processes in Solids*, edited by M. Ueta, H. Kanzaki, K. Kobayashi, Y. Toyozawa, and

E. Hanamura (Springer, Berlin, 1986), chap. 4.

<sup>2</sup> K. S. Song and R. T. Williams, *Self-Trapped Excitons*

- (Springer, Berlin, 1993).
- <sup>3</sup> A. Sumi, *J. Phys. Soc. Jpn.* **43**, 1286 (1977).
  - <sup>4</sup> W. L. Faust, *Science* **245**, 37 (1989).
  - <sup>5</sup> J.-M. Spaeth, J. R. Niklas, and R. H. Bartram, *Structural Analysis of Point Defects in Solids* (Springer, Berlin, 1992).
  - <sup>6</sup> J. F. Verwey, *J. Phys. Chem. Solids* **31**, 163 (1970).
  - <sup>7</sup> W. C. De Gruijter and T. Bokx, *J. Solid State Chem.* **6**, 271 (1973).
  - <sup>8</sup> G. Liidja and V. Plekhanov, *J. Lumin.* **6**, 71 (1973).
  - <sup>9</sup> M. Iwanaga, M. Watanabe, and T. Hayashi, *J. Lumin.* **87-89**, 287 (2000).
  - <sup>10</sup> M. Iwanaga, M. Watanabe, and T. Hayashi, *Phys. Rev. B* **62**, 10766 (2000).
  - <sup>11</sup> R. H. Silsbee, in *Electron Paramagnetic Resonance*, edited by S. Geschwind (Plenum Press, New York, 1972), chap. 7.
  - <sup>12</sup> D. Schoemaker, *Phys. Rev. B* **7**, 786 (1973).
  - <sup>13</sup> M. Nishi, H. Hara, Y. Ueda, and Y. Kazumata, *J. Phys. Soc. Jpn.* **42**, 1900 (1977).
  - <sup>14</sup> M. Nizam, Y. Bouteiller, B. Silvi, C. Pisani, M. Causa, and R. Dovesi, *J. Phys. C* **21**, 5351 (1988).
  - <sup>15</sup> M. Fujita, M. Itoh, Y. Bokumoto, H. Nakagawa, D. L. Alov, and M. Kitaura, *Phys. Rev. B* **61**, 15731 (2000).
  - <sup>16</sup> D. Schoemaker and J. L. Kolopus, *Solid State Commun.* **8**, 435 (1970).
  - <sup>17</sup> S. V. Nistor, E. Goovaerts, and D. Schoemaker, *Phys. Rev. B* **48**, 9575 (1993).
  - <sup>18</sup> T. Hirota, T. Fujita, and Y. Kazumata, *Jpn. J. Appl. Phys., Part 1* **32**, 4674 (1993).
  - <sup>19</sup> S. V. Nistor, E. Goovaerts, M. Stefan, and D. Schoemaker, *Nucl. Instrum. Methods Phys. Res. B* **141**, 538 (1998).
  - <sup>20</sup> M. Iwanaga, M. Watanabe, and T. Hayashi, *Int. J. Mod. Phys. B* **15**, 3677 (2001).
  - <sup>21</sup> R. W. G. Wyckoff, *Crystal Structures*, 2nd ed. (Wiley, New York, 1963), vol. 1.
  - <sup>22</sup> A. F. Wells, *Structural Inorganic Chemistry*, 5th ed. (Clarendon Press, Oxford, 1984), p. 273.
  - <sup>23</sup> J. Arends and J. F. Verwey, *Phys. Status Solidi* **23**, 137 (1967).
  - <sup>24</sup> W. C. De Gruijter and J. Kerssen, *J. Solid State Chem.* **5**, 467 (1972).
  - <sup>25</sup> J. Kerssen, W. C. De Gruijter, and J. Volger, *Physica (Amsterdam)* **70**, 375 (1973).
  - <sup>26</sup> M. Iwanaga, (unpublished).
  - <sup>27</sup> C. P. Slichter, *Principals of Magnetic Resonance*, 3rd ed. (Springer, Berlin, 1990), chap. 11.
  - <sup>28</sup> D. Schoemaker, *Phys. Rev.* **174**, 1060 (1968).
  - <sup>29</sup> I. Heynderickx, E. Goovaerts, and D. Schoemaker, *Phys. Rev. B* **36**, 1843 (1987).
  - <sup>30</sup> J. F. Verwey and J. Schoonman, *Physica (Amsterdam)* **35**, 386 (1967).
  - <sup>31</sup> J. Oberschmidt and D. Lazarus, *Phys. Rev. B* **21**, 5813 (1980).